PCCP

Accepted Manuscript




ROYAL SOCIETY OF CHEMISTRY

www.rsc.org/pccp

Journal Name

ARTICLE

# Facet-dependent activity and stability of $Co_3O_4$ nanocrystals towards the oxygen evolution reaction

Received 00th January 20xx,
Accepted 00th January 20xx

DOI: 10.1039/x0xx00000x

www.rsc.org/

Zhu Chen,[a] Coleman X. Kronawitter[a] and Bruce E. Koel[a]

The electrocatalytic activities and stabilities of spinel cobalt oxides with different morphologies have been investigated for the oxygen evolution reaction (OER) in an alkaline environment. Spinel cobalt oxide nanoparticles with well-defined cubic and octahedral morphologies were prepared, which predominantly expose the (100) and (111) surfaces, respectively. The OER activity of spinel cobalt oxide, measured in terms of current density, increases with higher relative proportion of the (111) surface, which can be attributed to the higher density of cobalt ions on the (111) surface compared to that on the (100) surface. The surfaces of cobalt oxide nanocubes are slighted reduced compared to those of nanooctahedra prior to OER testing. Based on chronoamperometry experiments, the nanocubes exhibited higher stability compared to the nanooctahedra, which could be due to the lower surface energy of the (100) surface compared to the (111) surface. The dependence of OER activity and stability on spinel cobalt oxide crystal facets demonstrates the importance of surface orientation in catalyst performance optimization.

## 1. Introduction

Efficiently driving the oxygen evolution reaction (OER) is a key barrier in various electrochemical devices, including metal–air batteries, water splitting cells, and electrolyzers.[1-4] In alkaline media, the OER involves the transfer of four electrons and typically requires high overpotential. As a result, active, stable, and affordable OER catalysts are highly sought after. Precious metal oxides such as iridium and ruthenium oxides are widely investigated OER catalysts due to their high activity.[5-7] However, the high costs associated with precious metals prevent commercial-scale applications, and further motivates research to develop cheaper alternatives. One promising candidate is spinel cobalt oxide ($Co_3O_4$) due to its high activity towards OER, corrosion resistance in alkaline environments, and elemental abundance.

Various factors can influence the performance of the OER catalyst, including crystallinity,[8-10] chemical composition,[11-13] and the inclusion of dopant atoms.[2,14] However, the influence of crystal facet exposure on the OER performance of $Co_3O_4$ catalysts in alkaline condition has not been reported. The exposure of different crystal facets to the electrolyte can have significant influence on catalyst performance due to their associated different arrangements and distributions of surface atoms. For example, Hu et al. reported that the highest activity for methane combustion was associated with the (112) crystal planes followed by the (011) and (001) planes.[15] In another account, Xie et al. demonstrated that the use of $Co_3O_4$ nanorods that predominantly expose (110) crystal surfaces lowers CO oxidation temperature.[16] Other studies on facet-dependent lithium ion charge capacity and heavy metal ion adsorption affinity have also demonstrated the significant influence of different crystallographic planes of $Co_3O_4$.[17, 18] In the study herein, we report on the facet dependence of OER activity and stability of $Co_3O_4$ in an alkaline medium. $Co_3O_4$ nanocrystals with various morphologies, including cubic, truncated octahedra, and octahedra were synthesized by hydrothermal synthesis. Nanocubes preferentially expose (100) crystal surfaces of the $Co_3O_4$ spinel structure whereas (111) crystal surfaces dominate on nanooctahedra.

## 2. Experimental

### 2.1 Synthesis

The $Co_3O_4$ nanocrystals of different facet exposure were prepared by a hydrothermal method.[17] Briefly, cobalt nitrate hexahydrate ($Co(NO_3)_2 \bullet 6H_2O$, 99%, Adrich) was dissolved in de-ionized water followed by drop-wise addition of sodium hydroxide (NaOH, 98%, Adrich). The mixture was transferred into a Teflon-lined autoclave and heated to 180 °C for 5 hours. The product was centrifuged and washed with de-ionized water and acetone and then dried overnight in a vacuum oven at 60 °C. Finally the $Co_3O_4$ nanocrystals were calcined at 450 °C for 5h. The $Co_3O_4$ nanocubes were obtained with a 8:1 molar ratio of cobalt nitrate to sodium hydroxide and the ratio for

[a] Department of Chemical and Biological Engineering, Princeton University, Princeton, NJ 08544.

† Electronic Supplementary Information (ESI) available: Raman spectroscopy, XPS, BET surface area, capacitance measurement, synthesis details and XPS peak area quantification of $Co_3O_4$. See DOI: 10.1039/x0xx00000x

nanooctahedra synthesis was 4:1. The concentration of the reagents used during synthesis is included in the supplementary information (Table S1).

### 2.2 Structure Characterization

Scanning electron microscopy (SEM, Quanta 200 FE-ESEM) was used to investigate the morphology of $Co_3O_4$ nanocrystals. Transmission electron microscopy (TEM, Philips CM200 FEG-TEM) was used to investigate the morphology of Co3O4 and to obtain electron diffraction patterns. X-ray diffraction (XRD, Rigaku Miniflex XRD) and Raman spectroscopy (Horiba LabRAM Aramis) were used to identify the crystal structure and local crystallinity of $Co_3O_4$ nanocrystals. The surface elemental composition was characterized using X-ray photoelectron spectroscopy (XPS, SPECS PHOIBOS 100-5 MCD) using a pass energy of 20 eV and an Al Kα X-ray source operated at 200 W. BET analysis (Micrometrics ASAP 2010) was performed to determine the surface area of the nanocrystals in powder form.

### 2.3 Electrochemical Characterization

Electrochemical evaluation was performed using rotating disc electrode voltammetry (RDE). $Co_3O_4$ nanocrystals were dispersed in a 50%-50% volume mixture of de-ionized water and ethanol containing 0.2 wt% of Nafion® solution (LIQUION® LQ-1115). After sonication, the working electrode was prepared by depositing 20 µL of catalyst solution onto a glassy carbon electrode (PINE Research Instrument, 5 mm diameter) to achieve catalyst loadings of approximately 0.50 $mgcm^{-2}$. The working electrode along with a platinum wire counter electrode and a double-junction Ag/AgCl reference electrode were immersed in 0.1 M KOH electrolyte to perform cyclic voltammetry (CV) and linear sweep voltammetry (LSV) at scan rates of 50 and 1 $mVs^{-1}$, respectively. Chronoamperometry was performed by applying a constant electrode potential of 0.74 vs. Ag/AgCl to investigate the stability of different $Co_3O_4$ catalysts. Hereafter, the potentials measured vs. the Ag/AgCl electrode were converted to the reversible hydrogen electrode (RHE) scale. Capacitance measurement where carried out in 0.1 M tetrabutylammonium hexafluorophosphate in acetonitrile over a small potential window of ± 20 mV around the open circuit potential. The scan rates used in the capacitance measurements were 50, 100, 150, 200, 250, 300 and 400 mV/s. Rotating ring disk electrode (RRDE) voltammetry was performed using a glassy carbon electrode with a platinum ring (PINE Research Instrument, E6 Series). $Co_3O_4$ nanocrystals were deposited on the glassy carbon portion of the RRDE to achieve 0.5 $mgcm^{-2}$ catalyst loading, and the potential was swept from 0 to 1 V vs. Ag/AgCl at 20 $mVs^{-1}$. The platinum ring was held at a constant potential of -0.5 V vs. Ag/AgCl. Platinum wire and Ag/AgCl electrodes were used as counter and reference electrodes, respectively, and the solution was purged with $N_2$ gas for 20 min prior to RRDE experiments.

## 3. Results and Discussion

X-ray diffraction patterns of calcined $Co_3O_4$ nanocrystals are shown in Figure 1. The peaks in the XRD patterns can be assigned to planes of spinel $Co_3O_4$ (JCPDS 71-0816).[19] No other impurity peaks were present, indicating high purity of the prepared material (catalysts). Compared to the nanocubes, slight shifts in XRD peaks towards higher 2θ are observed for truncated nanocubes, and truncated nanooctahedra. However, all peaks were shifted by the same amount; therefore, the shifts are unlikely due to structural variation. We note that the XRD patterns do not show stronger intensities for the (100) or (111) reflections over others for these nanocrystals since they are randomly oriented with respect to each other.

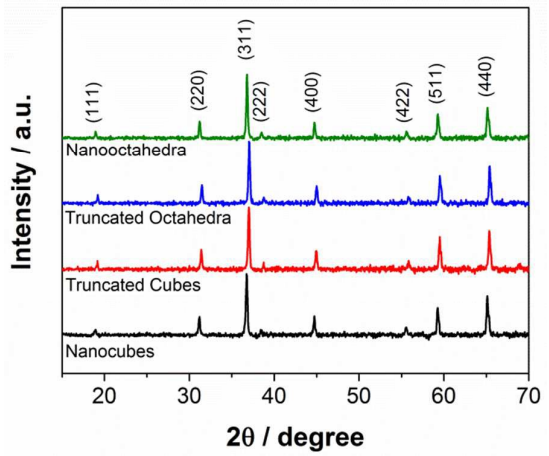


Figure 1. X-ray diffraction patterns of $Co_3O_4$ nanocubes, truncated nanocubes, truncated nanooctahedra, and nanooctahedra.

SEM images in Figure 2 are illustrative of the morphologies of the various $Co_3O_4$ nanocrystals. Given the crystal structure of this material, it is clear that $Co_3O_4$ nanocubes predominantly expose (100) crystal planes (Figure 2a) and $Co_3O_4$ nanooctahedra expose (111) crystal planes (Figure 2d).

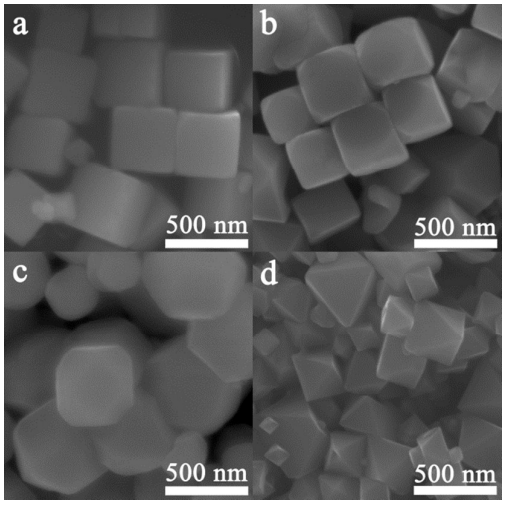


Figure 2. SEM images of a) $Co_3O_4$ nanocubes, b) truncated nanocubes, c) truncated nanooctahedra, and d) nanooctahedra.

Particle sizes of the nanocrystals were between 100 - 500 nm. By increasing the NaOH concentration during the synthesis, the relative proportion of (111) surfaces to (100) surfaces was increased as illustrated in Figures 2b and 2c. The final morphology of face centred cubic (fcc) nanocrystal is controlled by the relative growth rate, R, along the <001> and <111> directions, where a higher R value is correlated with formation of octahedral morphologies.[20] By increasing NaOH concentration during the synthesis, $Na^+$ ions that preferentially attach on the (111) surface slow down the growth rate in the <111> direction, which results in the formation of $Co_3O_4$ nanooctahedra. A similar observation has been reported in a previous paper.[21] Raman spectra (Figure S1) further confirm the formation of spinel $Co_3O_4$ nanocrystals with good local crystallinity. All vibrational features can be assigned to the Raman active $A_{1g}$, $E_g$ and $F_{2g}$ modes.[22] TEM images of $Co_3O_4$ nanocubes and nanooctahedra are shown in Figure 3, along with the selected area electron diffraction (SAED) from single catalyst particles to illustrate the diffraction pattern in the [001] and [111] directions. From the diffraction pattern we can conclude that the exposed facets of the nanocubes and nanooctahedra are the (100) and (111) surfaces, respectively. Crystal structure models of the $Co_3O_4$ unit cell and the (100) and (111) surfaces are included in the Supplementary Information (Figure S2).

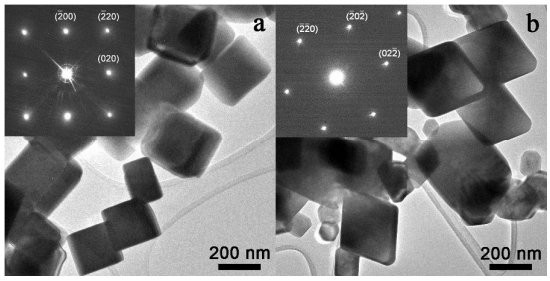


Figure 3. TEM images of $Co_3O_4$ (left) nanocubes and (right) nanooctahedra. Insets show the SAED diffraction patterns along the [001] and [111] directions.

XPS analysis of $Co_3O_4$ nanocrystals in powder form was performed prior to electrochemical testing to probe the near-surface chemical composition and chemical state of the different catalysts. For $Co_3O_4$, Co 2p XPS spectra (Figure S3) show two spin-orbit split lines with the $2p_{3/2}$ peak at 780.1 eV and the $2p_{1/2}$ peak at 795.3 eV, separated by 15.2 eV.[23-24] The same chemical information can be obtained from both spin-orbit split peaks, as a result, line-shape analysis was only carried out on the larger $2p_{3/2}$ peak. Peak fitting of the Co $2p_{3/2}$ spectra was carried out in accord with a recent paper by Biesinger et al.[25] In Figure 4, peaks at 779.8, 781.1, 782.4, 785.1 and 789.1 eV are attributed $Co^{2+}$ and $Co^{3+}$ ions. The first component is due to the main photoelectron lines from $Co^{2+}$ and $Co^{3+}$ ions, and the other component peaks are due to satellite shake-up peaks from either $Co^{2+}$ or $Co^{3+}$ ions. Based on the study by Yang et al., two peaks at 780.7 and 782.5 eV are observed for $Co(OH)_2$, which contains only $Co^{2+}$ species.[26] Furthermore, for CoO(OH), which contains only $Co^{3+}$ species, two peaks at 780.4 eV and 781.7 eV are observed.[26] This indicates that both $Co^{2+}$ and $Co^{3+}$ contribute to the peak at 779.8 eV observed in Figure 4, and the peaks at 781.1 and 782.4 eV are attributed to $Co^{3+}$ and $Co^{2+}$, respectively. Detailed XPS fitting parameters are included in the Supplementary Information (Table S3).

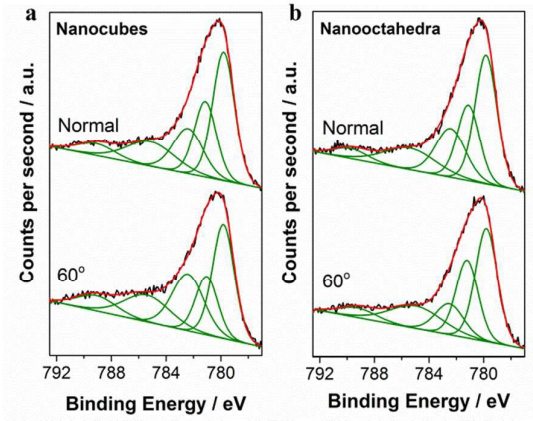


Figure 4. Co $2p_{3/2}$ XPS spectra of (a) $Co_3O_4$ nanocube modified electrodes, and (b) nanooctahedra modified electrodes at both normal and 60° off-normal photoelectron takeoff angles.

Co $2p_{3/2}$ spectra of $Co_3O_4$ nanocubes and nanooctahedra obtained at normal take-off angle were very similar. However, for nanocube spectra taken at a 60° takeoff angle, the relative intensity of the $Co^{2+}$ peak at 782.4 eV compared to the total Co $2p_{3/2}$ signal was much higher than when taken at normal emission. The probe depth in XPS collecting photoelectrons at a 60° takeoff angle is smaller than for collecting at normal emission, which indicates a higher $Co^{2+}$ concentration at or closer to the surface of the $Co_3O_4$ nanocubes. In contrast, the Co $2p_{3/2}$ XPS spectra of the $Co_3O_4$ nanooctahedra showed little difference between normal and 60° takeoff angles, which indicates little variation in the $Co^{2+}$ and $Co^{3+}$ concentrations in the near surface region.

OER activity of $Co_3O_4$ nanocrystals was evaluated by LSV in 0.1 M KOH solution at 1 $mV/s^{-1}$ scan rate, as shown in Figure 5. $Co_3O_4$ nanocubes and nanooctahedra exhibited significantly different OER activity despite similar chemical compositions; the same calcination procedure; and similar catalyst loading $Co_3O_4$ on the working electrode. Based on the polarization curves shown in Figure 5, $Co_3O_4$ nanooctahedra exhibited 45% greater current density at 1.96 V vs. RHE compared to that of the nanocubes. To confirm the production of $O_2$, RRDE voltammetry experiments were performed (Figure S4). From RRDE experiments, the Faradaic efficiency for the $Co_3O_4$ nanocubes and nanooctahedra toward $O_2$ production was found to be 83.3% and 82.1% at 1.7 V vs. RHE, which indicates that $O_2$ was the major product of the OER reaction. To rule out the effects of particle size and electrode surface area on this OER activity, BET surface area and capacitance measurements were performed. Based on the BET analysis, particle surface areas for the $Co_3O_4$ nanocubes and nanooctahedra were 4.5 and 3.7 $m^2g^{-1}$, respectively (Figure S5). In double-layer

capacitance measurements, similar specific capacitance values were obtained (Figure S6), which indicates similar electrode roughness factors.[27] Similar surface areas and electrode roughness factors in conjunction with higher nanooctahedra activity establish that the (111) surfaces of $Co_3O_4$ are more active than the (100) surfaces in alkaline conditions.

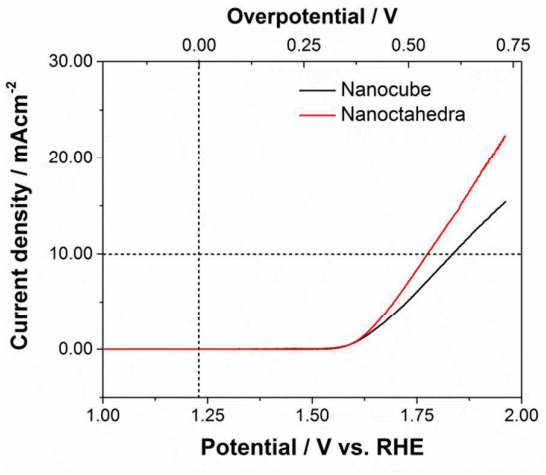


Figure 5. Linear sweep voltammetry of $Co_3O_4$ nanocubes and nanooctahedra. The current density at 1.96 V vs. RHE is 15.4 and 22.2 $mAcm^{-2}$ for nanocubes and nano-octahedra, respectively. Scan obtained at 1 $mVs^{-2}$

Building on the LSV result, we expect the OER activity of $Co_3O_4$ nanocrystals to increase with increasing proportion of exposed (111) surface. This is indeed what we observed when comparing the CV results of various $Co_3O_4$ nanocrystals taken at 50 $mVs^{-1}$ scan rate. As the morphology of the $Co_3O_4$ nanocrystal changes from cubic to octahedral, the proportion of the (111) surface exposed increases. From the CV data in Figure 6, it is clear that the maximum current density at 1.96 V vs. RHE increases in line with the proportion of exposed (111) surface. This clear trend further emphasizes the importance of (111) surface towards OER activity.

In recent studies of OER reaction mechanisms on cobalt oxides, surface Co ions have been proposed as the active site for OER.[28-29] According to these proposals, the oxidation state of cobalt increases during OER. As a result, the density and oxidation state of surface cobalt ions are critical for OER activity. From the inset of Figure 6, two redox peaks can be identified for $Co_3O_4$ nanocubes and nanooctahedra. The first peak located at 1.25 V corresponds to the oxidation of $Co^{2+}$ to $Co^{3+}$, and the latter peak at 1.46 - 1.50 V corresponds to $Co^{3+}$ to $Co^{4+}$ oxidation.[30] Under the same scan rate, a much larger redox current density was observed for the nanooctahedra compared to that of the nanocubes. Since the redox current density is associated with the change in the oxidation state of surface Co ions, a larger value indicates a higher density of Co ions on (111) surfaces compared to (100) surfaces. Previous work shows that $Co^{2+}$ and $Co^{3+}$ ions are both present at higher concentration on the (111) surface than on the (100) surface. From studies of Xiao et al., the number of $Co^{2+}$ ions per unit cell on the (100) and (111) surfaces is calculated to be 2 and 3.75, respectively.[17] In addition, using DFT calculations, Su et al. have shown a higher density of $Co^{3+}$ dangling bonds on the (111) surfaces (27.7 $Å^{-2}$) compared to that on the (100) surfaces (8.68 $Å^{-2}$) and proposed that the density of $Co^{3+}$ ions in octahedral sites is critical for the catalytic performance of different $Co_3O_4$ surfaces.[31]. From Our XPS results taken at 60° takeoff geometry revealed a larger proportion of $Co^{3+}$ in the near surface region for $Co_3O_4$ nanooctahedra compared to nanocubes, which is in good agreement with our CV data and the DFT calculations from Su et al.[31] Therefore, the higher OER activity of $Co_3O_4$ nanooctahedra can be attributed to the higher density of $Co^{3+}$ ions on the (111) surface. In addition to the higher $Co^{3+}$ density, DFT calculations of water adsorption on $Co_3O_4$ have shown that water molecules dissociate when adsorbed on the (111) surface, forming Co-OH groups, whereas, molecular adsorption is favoured on the (100) surface.[32] The surface Co(OH) groups are the starting point of the water oxidation cycle and they can be transformed into $Co^{4+}$ oxo sites and subsequently form hydroperoxide and other intermediates. Consequently, the higher reactivity for water dissociation on (111) surfaces could also contribute to the higher OER activity of $Co_3O_4$ nanooctahedra.

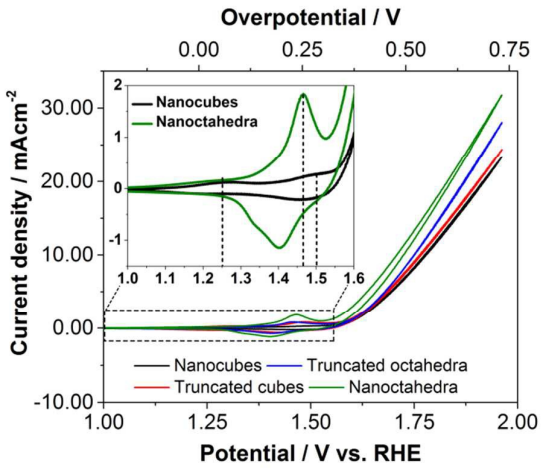


Figure 6. Cyclic voltammetry of Co3O4 nanocrystals at 50 $mVs^{-1}$. Inset showing the redox peaks at 1.25 and 1.46 - 1.5 V.

Recently, Zhang et al. have observed two different catalytic sites on $Co_3O_4$ surfaces: a kinetically fast site consists of two $Co^{III}$-OH surface species bridged by an O atom, and a slow site associated with formation of isolated $Co^{IV}$=O surface species.[33] Given the higher surface density of Co ions on (111) surfaces over the (100) surfaces, and the high activity of (111) surfaces for water dissociation, it is possible that there is a higher density of the fast catalytic site on the (111) crystal plane. Tafel analysis (Figure 7) was carried out to investigate the kinetics of water oxidation on different $Co_3O_4$ nanocrystals. In the low current density regime, the Tafel slope of $Co_3O_4$ nanocubes and nanooctahedra was approximately 60 $mVdec^{-1}$, which is a value commonly observed for metal oxide catalysts in alkaline solution.[30, 34-35] Similar values of the Tafel slopes for

the nanocubes and nanooctahedra in the low current density region indicate a similar OER mechanism, possibly involving a reversible one-electron transfer prior to a chemical turnover-limiting step.[36] At 0.4 V overpotential, there is a bend in the Tafel curve followed by an increase in the value of the Tafel slope. A similar behaviour of the Tafel slope as a function of overpotential has been observed for the $RuO_2$ (110) surface, which was attributed in that case to the change in the electrochemically stable surface from a mixed OH/O termination to a purely O-terminated surface.[37] A similar surface change could take place for these $Co_3O_4$ catalysts, since several studies have proposed and observed the formation of $Co^{IV}$=O surface groups on $Co_3O_4$ surfaces during OER.[33, 38]

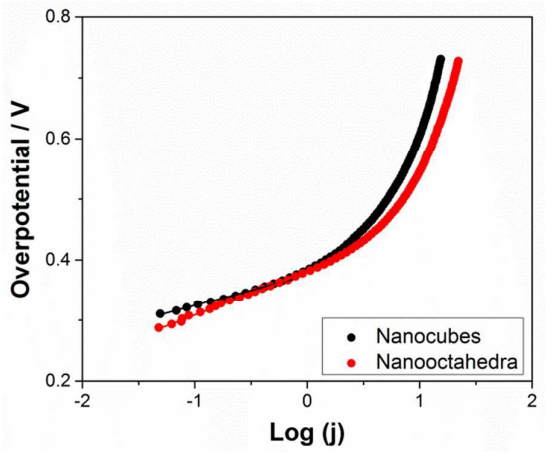


Figure 7. Tafel plot of $Co_3O_4$ nanocubes and nanooctahedra. The Tafel slope of nanocubes and nanooctahedra is 59 and 67 $mVdec^{-1}$, respectively.

In addition to the activity, we sought to assess the OER stability of the different $Co_3O_4$ crystal surfaces. Chronoamperometry was performed by applying a constant working electrode potential at 0.75 V vs. Ag/AgCl, as shown in Figure 8. Very stable performance was obtained from chronoamperometry for the nanocubes, where only a 11% decrease in current density was observed. For the $Co_3O_4$ nanooctahedra, a 19% decrease in current density was observed. The stability results are expected from the standpoint of the higher calculated surface energy of the (111) surface compared to the (100) surface.[39] Similar results demonstrating this inverse trend in activity and stability of the different crystal orientations of perovskite $SrRuO_3$ catalysts have been observed.[40]

Raman spectroscopy (Figures 9a and 9b) of $Co_3O_4$ nanocubes and nanooctahedra before and after chronoamperometry are very similar and show only slight (~1 $cm^{-1}$) shifts in peak positions. The lack of new Raman features indicates no bulk material changes take place during the duration of the stability tests. XPS Co $2p_{3/2}$ spectra before and after the stability tests are shown in Figures 9c and 9d. The Co $2p_{3/2}$ spectra before and after stability tests are nearly identical for all the $Co_3O_4$ nanocrystals, which indicates no change in the surface cobalt species as probed by XPS.

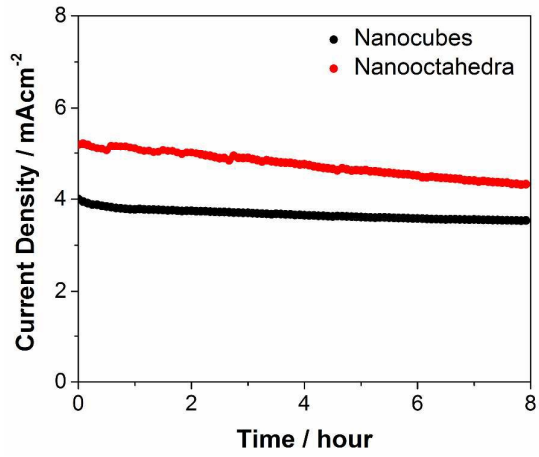


Figure 8. Chronoamperometry of $Co_3O_4$ nanocubes and nanooctahedra modified electrodes in 0.1M KOH solution at 1.7 V vs. RHE.

Based on the combined Raman and XPS analysis, we conclude that no measurable change in the elemental composition and local crystallinity took place on the (100) and (111) surfaces during the stability tests. However, recent studies have reported the formation of a few nanometers thick amorphous layer on the surface of OER catalysts.[19, 41] Such amorphous layer could be a possible mechanism for the degradation of the $Co_3O_4$ nanocrystals observed from the stability tests and might be a reason for the minimal changes observed in the Raman and XPS spectra taken post-degradation.

## 4. Conclusion

We investigated the role of the surface structure of spinel Co3O4, as probed by varying the exposure of crystal facets in nanoparticulate electrodes, on the activity and stability of these catalysts for OER in alkaline media. It was determined that OER activity increased with a higher proportion of (111) surface exposure. Based on linear sweep voltammetry data, nanooctahedra exposing predominantly (111) surfaces were associated with 45% greater current density for water oxidation than nanocubes, which expose predominantly (100) surfaces. Chronoamperometry showed 5% and 10% decreases in current densities for $Co_3O_4$ nanocubes and nanooctahedra, respectively. The higher activity of (111) surfaces was discussed in the context of several proposed mechanisms. Most notably, the higher activity of (111) surfaces could be a consequence of its higher Co ion density and higher reactivity toward water dissociation. The higher stability of (100) surfaces is attributed to the lower surface energy for this face. Our study indicates the importance of crystal orientation and faceting on the activity and stability of spinel $Co_3O_4$ catalysts for OER, and that tailoring and controlling this property is an

important consideration when optimizing catalyst performance.

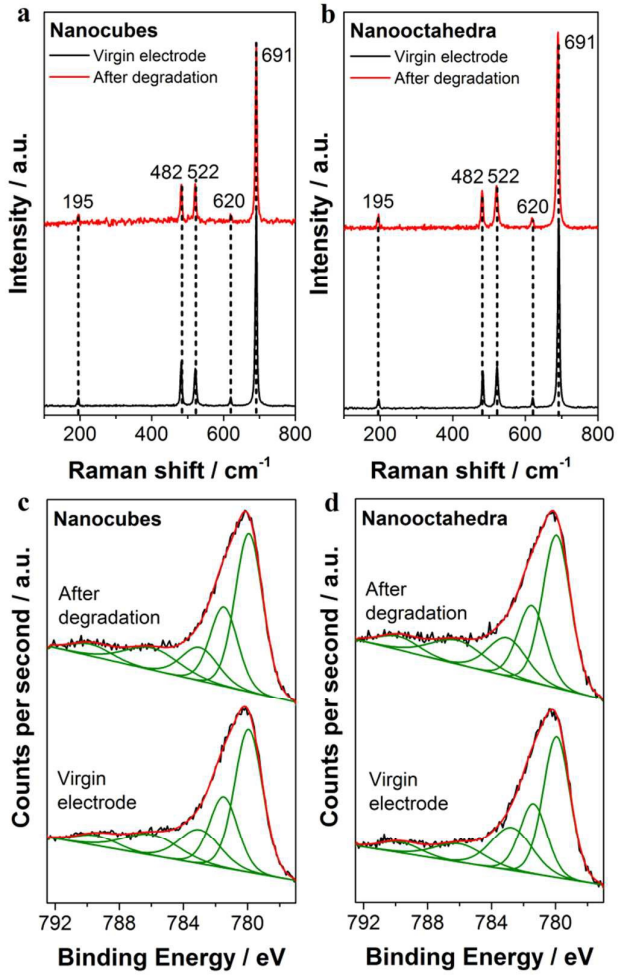


Figure 9. Raman spectroscopy of (a) $Co_3O_4$ nanocubes and (b) nanooctahedra before and after a stability test in $N_2$-saturated 0.1 M KOH solution. Co $2p_{3/2}$ XPS spectra of (c) $Co_3O_4$ nanocube modified electrode and (d) nanooctahedra modified electrode before and after stability testing. These XPS spectra were obtained at a photoelectron takeoff angle along the surface normal.

## Acknowledgements

Z.C. acknowledges support by a Natural Sciences and Engineering Research Council of Canada (NSERC) Postgraduate Scholar-ship. This work was supported by the Addy/ISN North American Low Carbon Emission Energy Self-Sufficiency Fund of the Andlinger Center for Energy and the Environment (ACEE) at Princeton University. Z.C. acknowledges the assistance of Dr. Nan Yao with the TEM experiments.

## Notes and references

1 S. D. Song, H. M. Zhang, X. P. Ma, Z. G. Shao, R. T. Baker and B. L. Yi, Int. J. Hydrogen Energy, 2008, **33**, 4955-4961.

2 J. Suntivich, K. J. May, H. A. Gasteiger, J. B. Goodenough and Y. Shao-Horn, Science, 2011, **334**, 1383-1385.

3 H. Inoue, T. Shimada, Y. Kou, Y. Nabetani, D. Masui, S. Takagi and H. Tachibana, Chemsuschem, 2011, **4**, 173-179.

4 L. X. Zhang, S. L. Zhang, K. J. Zhang, G. J. Xu, X. He, S. M. Dong, Z. H. Liu, C. S. Huang, L. Gu and G. L. Cui, Chem. Commun. (Cambridge, U. K.), 2013, **49**, 3540-3542.

5 Y. Lee, J. Suntivich, K. J. May, E. E. Perry and Y. Shao-Horn, J. Phys. Chem. Lett., 2012, **3**, 399-404.

6 T. Reier, M. Oezaslan and P. Strasser, ACS Catal., 2012, **2**, 1765-1772.

7 K. Sardar, E. Petrucco, C. I. Hiley, J. D. B. Sharman, P. P. Wells, A. E. Russell, R. J. Kashtiban, J. Sloan and R. I. Walton, Angew. Chem. Int. Edit., 2014, **53**, 10960-10964.

8 S. Cherevko, T. Reier, A. R. Zeradjanin, Z. Pawolek, P. Strasser and K. J. Mayrhofer, Electrochem. Commun., 2014, **48**, 81-85.

9 H. F. Jia, J. Stark, L. Q. Zhou, C. Ling, T. Sekito and Z. Markin, RSC Adv., 2012, **2**, 10874-10881.

10 T. Reier, D. Teschner, T. Lunkenbein, A. Bergmann, S. Selve, R. Kraehnert, R. Schlogl and P. Strasser, J. Electrochem. Soc., 2014, **161**, F876-F882.

11 M. Hamdani, R. N. Singh and P. Chartier, Int. J. Electrochem. Sci., 2010, **5**, 556-577.

12 J. P. Singh and R. N. Singh, J New Mat. Elect. Syst., 2000, **3**, 137-145.

13 T. C. Wen and H. M. Kang, Electrochim. Acta, 1998, **43**, 1729-1745.

14 L. Trotochaud, S. L. Young, J. K. Ranney and S. W. Boettcher, J. Am. Chem. Soc., 2014, **136**, 6744-6753.

15 L. H. Hu, Q. Peng and Y. D. Li, J. Am. Chem. Soc., 2008, **130**, 16136-16137.

16 X. W. Xie, Y. Li, Z. Q. Liu, M. Haruta and W. J. Shen, Nature, 2009, **458**, 746-749.

17 X. L. Xiao, X. F. Liu, H. Zhao, D. F. Chen, F. Z. Liu, J. H. Xiang, Z. B. Hu and Y. D. Li, Adv. Mater. (Weinheim, Ger.), 2012, **24**, 5762-5766.

18 X. Y. Yu, Q. Q. Meng, T. Luo, Y. Jia, B. Sun, Q. X. Li, J. H. Liu and X. J. Huang, Sci Rep-Uk, 2013, **3**, 2886.

19 H. F. Liu and G. R. Patzke, Chem-Asian J, 2014, **9**, 2249-2259.

20 Z. L. Wang, J. Phys. Chem. B, 2000, **104**, 1153-1175.

21 B. Y. Geng, F. M. Zhan, C. H. Fang and N. Yu, J. Mater. Chem., 2008, **18**, 4977-4984.

22 V. G. Hadjiev, M. N. Iliev and I. V. Vergilov, J Phys. C Solid State, 1988, **21**, L199-L201.

23 M. Burriel, G. Garcia, J. Santiso, A. Abrutis, Z. Saltyte and A. Figueras, Chem. Vap. Deposition, 2005, **11**, 106-111.

24 C. A. F. Vaz, D. Prabhakaran, E. I. Altman and V. E. Henrich, Phys. Rev. B, 2009, **80**, 155457.

25 M. C. Biesinger, B. P. Payne, A. P. Grosvenor, L. W. M. Lau, A. R. Gerson and R. S. Smart, Appl. Surf. Sci., 2011, **257**, 2717-2730.

26 J. Yang, H. W. Liu, W. N. Martens and R. L. Frost, J. Phys. Chem. C, 2010, **114**, 111-119.

27 J. A. Koza, Z. He, A. S. Miller and J. A. Switzer, Chem. Mater., 2012, **24**, 3567-3573.

28 M. Garcia-Mota, M. Bajdich, V. Viswanathan, A. Vojvodic, A. T. Bell and J. K. Norskov, J. Phys. Chem. C, 2012, **116**, 21077-21082.

29 M. Bajdich, M. Garcia-Mota, A. Vojvodic, J. K. Norskov and A. T. Bell, J. Am. Chem. Soc., 2013, **135**, 13521-13530.

30 F. Svegl, B. Orel, I. Grabec-Svegl and V. Kaucic, Electrochim. Acta, 2000, **45**, 4359-4371.
31 D. W. Su, S. X. Dou and G. X. Wang, Sci Rep-Uk, 2014, **4**, 5767.
32 F. Zasada, W. Piskorz, S. Cristol, J. F. Paul, A. Kotarba and Z. Sojka, J. Phys. Chem. C, 2010, **114**, 22245-22253.
33 M. Zhang, M. de Respinis and H. Frei, Nature Chem., 2014, **6**, 362-367.
34 R. L. Doyle and M. E. G. Lyons, Phys. Chem. Chem. Phys., 2013, **15**, 5224-5237.
35 Y. Y. Liang, Y. G. Li, H. L. Wang, J. G. Zhou, J. Wang, T. Regier and H. J. Dai, Nat. Mater., 2011, **10**, 780-786.
36 M. W. Kanan and D. G. Nocera, Science, 2008, **321**, 1072-1075.
37 K. A. Stoerzinger, L. Qiao, M. D. Biegalski and Y. Shao-Horn, J Phys. Chem. Lett., 2014, **5**, 1636-1641.
38 Y. Surendranath, M. W. Kanan and D. G. Nocera, J. Am. Chem. Soc., 2010, **132**, 16501-16509.
39 F. Zasada, W. Piskorz, P. Stelmachowski, A. Kotarba, J.-F. o. Paul, T. Płociński, K. J. Kurzydłowski and Z. Sojka, J Phys. Chem. C, 2011, **115**, 6423-6432.
40 S. H. Chang, N. Danilovic, K. C. Chang, R. Subbaraman, A. P. Paulikas, D. D. Fong, M. J. Highland, P. M. Baldo, V. R. Stamenkovic, J. W. Freeland, J. A. Eastman and N. M. Markovic, Nat. Commun., 2014, **5**, 4191.
41 K. J. May, C. E. Carlton, K. A. Stoerzinger, M. Risch, J. Suntivich, Y. L. Lee, A. Grimaud and Y. Shao-Horn, J Phys. Chem. Lett., 2012, **3**, 3264-3270.